Optimization of Geometrical Calibration in Pinhole SPECT

Dirk Bequé, *Student Member, IEEE,* Johan Nuyts, *Member, IEEE,* Paul Suetens, *Member, IEEE,* and Guy Bormans

***Abstract*— Previously, we developed a method to determine the acquisition geometry of a pinhole camera. This information is needed for the correct reconstruction of pinhole SPECT images. The method uses a calibration phantom consisting of three point sources and their positions in the field of view influence the accuracy of the geometry estimate. This study proposes two particular configurations of point sources with specific positions and orientations in the field of view for optimal image reconstruction accuracy. For the proposed calibration setups, inaccuracies of the geometry estimate due to noise in the calibration data, only cause sub-resolution inaccuracies in reconstructed images. The calibration method also uses a model of the point source configuration, which is only known with limited accuracy. The study demonstrates however, that, with the proposed calibration setups, the error in reconstructed images is comparable to the error in the phantom model.**

***Index Terms*— Pinhole, calibration, single photon emission computed tomography.**

I. Introduction

The reconstruction of pinhole SPECT data requires a correct description of the acquisition geometry of the pinhole camera. For a conventional pinhole system with a circular orbit of a planar detector, this geometry can be uniquely described by the seven parameters listed in Table I and shown in figure 1 [1]. The focal length f is the distance from the detector to the focal point of the pinhole system. The distance d and the mechanical offset m describe the distance from the focal point to the rotation axis (z axis) in the directions orthogonal (d) and parallel (m) to the detector plane. The tilt and twist angles, Φ and Ψ, further describe the orientation of the detector plane and the detector pixel grid (uv coordinate system) with respect to the axis of rotation. The tilt angle Φ is the angle between the detector and the rotation axis. The twist Ψ is the angle between the v axis and the orthogonal projection of the axis of rotation on the detector. The electrical shifts e_u and e_v finally relate the location of the origin of the detector pixel grid to its position in the projection image. This relation is specified as a collective translation of the pixel grid along its column (e_u) and row (e_v) directions. For a more extended discussion of these parameters, we refer to [1].

Previously, we developed a method to determine the above acquisition geometry from the SPECT acquisition of a calibration phantom consisting of three point sources [1]. The method can be considered as an extension of previous methods, estimating a subset of the above parameters, using one [2]–[5] or two [6] point sources. To estimate all 7 parameters, three point sources are necessary and sufficient, and a model of the point source configuration has to be available [1]. For most point source configurations, the knowledge of at least two of the distances between the point sources provides a sufficient model [1]. In the practical implementation, all three distances d_{12}, d_{13}, d_{23} between the point sources are taken into account in the phantom model [1], with $d_{ii'}$ being the distance between point source i and i'.

The method first acquires a pinhole SPECT scan of the three point sources and calculates the mass centers of their projections. The acquisition geometry is then determined by a least squares fit of estimated point source projection locations

Work supported by K.U.Leuven grant OT-00/32, F.W.O. grant G.0174.03, K.U.Leuven grant IDO/02/012 and I.W.T. grant SBO - ANIMONE.

D. Bequé and J. Nuyts are with the Dept. of Nuclear Medicine, K.U.Leuven, P. Suetens is with the Lab. for Medical Image Computing, K.U.Leuven, and G. Bormans is with the Lab. for Radiopharmaceutical Chemistry, K.U.Leuven. (e-mail: dirk.beque@uz.kuleuven.ac.be)

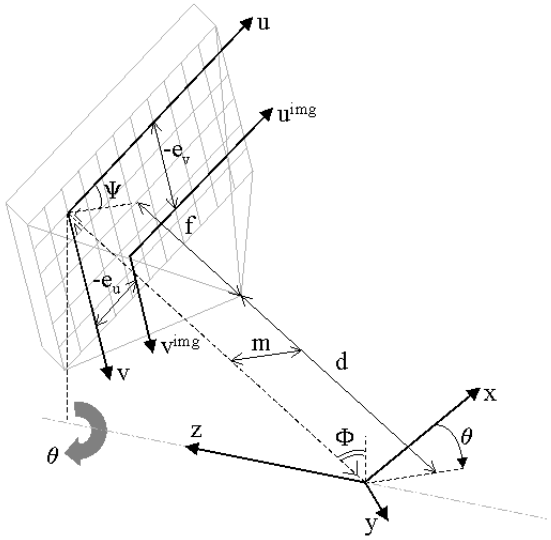

Fig. 1. Pinhole Camera Acquisition Geometry. The rotation of the detector during the acquisition is represented by θ.

TABLE I
PINHOLE PARAMETERS.

Symbol	Name
f	Focal length
d	Distance d
m	Mechanical offset
e_u e_v	Electrical shifts
Φ	Tilt angle
Ψ	Twist angle

TABLE II
CALIBRATION ENTITIES.

Name	# Parameters	Parameters	Description
Acquisition geometry	7	$f, d, m, e_u, e_v, \Phi, \Psi$	Geometry of the pinhole system.
Phantom configuration	3	d_{12}, d_{13}, d_{23}	Actual distances between the 3 calibration point sources.
Phantom model	3	$d'_{12}, d'_{13}, d'_{23}$	Values of the distances between the 3 point sources used in calculations.
Phantom position	6	$t_x, t_y, t_z, \rho_1, \rho_2, \rho_3$	Actual position & orientation of the phantom in the field of view.
Calibration setup	9	$d_{12}, d_{13}, d_{23}, t_x, t_y, t_z, \rho_1, \rho_2, \rho_3$ or $x_1, y_1, z_1, x_2, y_2, z_2, x_3, y_3, z_3$	Phantom configuration + Phantom position.

to the measured mass centers. Besides the 7 parameters of the acquisition geometry, the positions of the point sources are estimated as well, but not the distances between them. This is accomplished by specifying the point source coordinates by the 3 distances d_{12}, d_{13}, d_{23}, 3 rotations ρ_1, ρ_2, ρ_3 and 3 translations t_x, t_y, t_z. The distances d_{12}, d_{13}, d_{23} define the shape or configuration of the calibration phantom and remain fixed during the calibration. This rigid phantom is then correctly positioned in the field of view by the 3 rotations ρ_1, ρ_2, ρ_3 and the 3 translations t_x, t_y, t_z, and these rotations and translations have to be estimated by the calibration procedure.

With noisy calibration data, the acquisition geometry can only be estimated with limited accuracy. Both the configuration of the calibration phantom d_{12}, d_{13}, d_{23} and its position in the field of view $t_x, t_y, t_z, \rho_1, \rho_2, \rho_3$ influence this accuracy. In the remainder of this text, this combination of phantom configuration and phantom position will be referred to as 'calibration setup'. Additionally, the use of an incorrect phantom model $d'_{12}, d'_{13}, d'_{23}$ (instead of d_{12}, d_{13}, d_{23}) in the calibration calculations can degrade this accuracy even further. During reconstruction, the resulting errors on the acquisition geometry propagate into the reconstructed images, causing loss of spatial resolution and/or image deformation. The aim of this study is to determine an optimal calibration setup for accurate image reconstruction in practice, despite noise on the calibration data and phantom model errors. For clarity, table II provides an overview of the different entities involved in the calibration process.

II. METHOD

This section studies two sources of errors: noise on the calibration data and the use of an incorrect phantom model in the calibration calculations. Both sources of error result in errors on the calibration results, which, in turn, degrade the accuracy of image reconstruction by loss of spatial resolution and/or image deformation. First, analytical expressions for the projection of the calibration phantom are given. Next, these expressions are used to calculate linear systems, which allow us to evaluate the estimation accuracy as a function of the noise on the calibration data and/or the errors on the phantom model. Finally, the reconstruction accuracy is derived from this estimation accuracy by simulating and evaluating the reconstruction of a grid of point sources. For that purpose, however, the estimation accuracy results first have to be transformed into a more suitable representation.

A. Phantom Projection

The projection coordinates $U = (u_i(\theta), v_i(\theta))\ i=1,2,3$ of the three calibration point sources can be calculated analytically as a function of the projection angles θ, the acquisition geometry $f, d, m, e_u, e_v, \Phi, \Psi$ and the point source locations in Cartesian coordinates $x_i, y_i, z_i\ i=1,2,3$ [1].

$$u_i(\theta) = f\frac{m\ \cos\Psi - x'''_i}{d + y'''_i} + m\ \cos\Psi + e_u \tag{1}$$

$$v_i(\theta) = f\frac{m\ \sin\Psi - z'''_i}{d + y'''_i} + m\ \sin\Psi + e_v \tag{2}$$

in which

$$\begin{bmatrix} x'''_i \\ y'''_i \\ z'''_i \end{bmatrix} = R_3\, R_2\, R_1 \begin{bmatrix} x_i \\ y_i \\ z_i \end{bmatrix} \tag{3}$$

with

$$R_1 = \begin{bmatrix} cos\theta & sin\theta & 0 \\ -sin\theta & cos\theta & 0 \\ 0 & 0 & 1 \end{bmatrix} \tag{4}$$

$$R_2 = \begin{bmatrix} 1 & 0 & 0 \\ 0 & cos\Phi & -sin\Phi \\ 0 & sin\Phi & cos\Phi \end{bmatrix} \tag{5}$$

$$R_3 = \begin{bmatrix} cos\Psi & 0 & -sin\Psi \\ 0 & 1 & 0 \\ sin\Psi & 0 & cos\Psi \end{bmatrix} \tag{6}$$

As mentioned in the introduction, these Cartesian coordinates are transformed into a different set of coordinates $d_{12}, d_{13}, d_{23}, t_x, t_y, t_z, \rho_1, \rho_2, \rho_3$ to separate the phantom configuration d_{12}, d_{13}, d_{23} from the phantom position $t_x, t_y, t_z, \rho_1, \rho_2, \rho_3$. The transformation used in this text is

$$\begin{bmatrix} x_i \\ y_i \\ z_i \end{bmatrix} = \begin{bmatrix} t_x \\ t_y \\ t_z \end{bmatrix} + R_6\ R_5\ R_4 \begin{bmatrix} c_{xi} \\ c_{yi} \\ c_{zi} \end{bmatrix} \tag{7}$$

with

$$R_4 = \begin{bmatrix} cos\rho_1 & -sin\rho_1 & 0 \\ sin\rho_1 & cos\rho_1 & 0 \\ 0 & 0 & 1 \end{bmatrix} \tag{8}$$

$$R_5 = \begin{bmatrix} cos\rho_2 & 0 & -sin\rho_2 \\ 0 & 1 & 0 \\ sin\rho_2 & 0 & cos\rho_2 \end{bmatrix} \tag{9}$$

$$R_6 = \begin{bmatrix} cos\rho_3 & -sin\rho_3 & 0 \\ sin\rho_3 & cos\rho_3 & 0 \\ 0 & 0 & 1 \end{bmatrix} \tag{10}$$

and with

$$\begin{bmatrix} c_{x1} \\ c_{y1} \\ c_{z1} \end{bmatrix} = \begin{bmatrix} 0 \\ 0 \\ 0 \end{bmatrix}, \begin{bmatrix} c_{x2} \\ c_{y2} \\ c_{z2} \end{bmatrix} = \begin{bmatrix} d_{12} \\ 0 \\ 0 \end{bmatrix},$$
$$\begin{bmatrix} c_{x3} \\ c_{y3} \\ c_{z3} \end{bmatrix} = \begin{bmatrix} \frac{d_{12}^2+d_{13}^2-d_{23}^2}{2d_{12}} \\ \sqrt{d_{13}^2 - \left(\frac{d_{12}^2+d_{13}^2-d_{23}^2}{2d_{12}}\right)^2} \\ 0 \end{bmatrix}. \quad (11)$$

In words, this transformation first places the phantom in the field of view with point 1 in the xyz origin, point 2 on the positive x-axis and point 3 in the xy half plane of positive y coordinates. The phantom is then rotated 3 times ρ_1, ρ_2, ρ_3 to its correct orientation and eventually translated t_x, t_y, t_z to the correct position in the field of view.

B. Estimation Accuracy

The relations (1) to (11) define the projections of the calibration point sources $U = (u_i(\theta), v_i(\theta))\ i = 1, 2, 3$ as a function of the unknown calibration parameters P, which consist of both the pinhole acquisition geometry $f, d, m, e_u, e_v, \Phi, \Psi$ and the phantom position $t_x, t_y, t_z, \rho_1, \rho_2, \rho_3$. For small variations ΔP in these calibration parameters, we assume that the resulting projection coordinates U can also be approximated from the original projections U_0 by a linear system

$$U = U_0 + M\,\Delta P. \quad (12)$$

Here, M is a matrix containing the first order derivatives of the projection coordinates U, specified in (1) and (2), to each of the 13 parameters of P. The derivatives are evaluated for the original acquisition geometry and phantom position, yielding the projections U_0. Similar to the real calibration method, calibration of this linear system can be performed by solving (12) for the least square solution of ΔP. With $\Delta U = U - U_0$, this yields

$$\Delta P = (M^T M)^{-1} M^T \Delta U. \quad (13)$$

Expressed in this way, (13) allows us to calculate differences in the parameter estimates ΔP, due to specific changes of the projection coordinates ΔU. Noise on the projection coordinates, being the first source of error studied in this section, causes such differences ΔU. The noise is however better characterized by its covariance matrix $\mathrm{cov}(U)$ than by a single noise realization ΔU. This covariance matrix $\mathrm{cov}(U)$ is propagated through the linear estimator of (13), yielding the covariance matrix $\mathrm{cov}(P)$ of the estimated parameters P

$$\mathrm{cov}(P) = (M^T M)^{-1} M^T \mathrm{cov}(U)\, M (M^T M)^{-1}. \quad (14)$$

The effect of phantom model errors on the estimation accuracy, the second source of error, is studied in a two-step procedure. First the effect of small differences ΔX in the calibration setup $x_i, y_i, z_i\ \ i = 1, 2, 3$ (which change the phantom model d_{12}, d_{13}, d_{23} into $d'_{12}, d'_{13}, d'_{23}$) on the resulting point source projections U is simulated by the linear system

$$U = U_0 + N\,\Delta X \quad (15)$$

in which N is the matrix of the first order derivatives of the projection coordinates U, given in (1) and (2), to the Cartesian coordinates X of the calibration point sources. This system allows us to calculate the covariance matrix $\mathrm{cov}(U)$ due to random variations $\mathrm{cov}(X)$ of the calibration setup

$$\mathrm{cov}(U) = N \mathrm{cov}(X)\, N^T. \quad (16)$$

By substituting (16) now into (14), with M evaluated for the original phantom configuration d_{12}, d_{13}, d_{23}, the effects of the random variations of the phantom model $\mathrm{cov}(X)$ on the estimation accuracy $\mathrm{cov}(P)$ are eventually obtained.

Finally, the combined effects of noise on the calibration data and errors on the phantom model can easily be obtained by simply summing the covariance matrices $\mathrm{cov}(P)$ of the individual effects together.

C. Toward Reconstruction Accuracy

The covariance matrix $\mathrm{cov}(P)$ provides an excellent measure of the errors on the estimated parameters. In the next section however, the reconstruction accuracy will be evaluated and that evaluation starts from specific differences ΔP instead of a covariance matrix $\mathrm{cov}(P)$. If the errors on the different parameters of P were all independent (zero covariances), the effects of each parameter error $\Delta P_j = [0, ..., 0, 2\sigma_j, 0, ..., 0]^T\ \ j = 1, ..., 13$ could be evaluated individually. In this expression, σ_j represents the standard deviation of parameter j and a value of 2 standard deviations is chosen as a conservative, but realistic parameter error. A similar approach will here be followed. As shown in appendix I, the covariance matrix $\mathrm{cov}(P)$ can be decomposed as

$$\mathrm{cov}(P) = \Gamma\ \mathrm{cov}(Q)\ \Gamma^T = \Gamma\ I\ \Gamma^T = \Gamma\Gamma^T \quad (17)$$

in which I is the 13x13 identity matrix. (Note that this decomposition resembles an eigenvalue decomposition, but the columns of Γ do not have to form a set of normalized and orthogonal (eigen)vectors.) Consequently, there exists a set of errors ΔQ, which are independent of one another and which can be translated into the parameter errors ΔP by a linear transformation $\Delta P = \Gamma \Delta Q$. Each individual error $\Delta Q_j = [0, ..., 0, 2, 0, ..., 0]^T\ \ j = 1, ..., 13$ is now first transformed $\Delta P_j = \Gamma \Delta Q_j$ to the parameter errors ΔP and is then further processed as explained in the next section. Appendix I provides a recursive method to calculate Γ.

Finally note that the phantom position parameters $t_x, t_y, t_z, \rho_1, \rho_2, \rho_3$ are estimated during the calibration, but that they are not used in the reconstruction process. Consequently, they can be ignored in the evaluation of the reconstruction accuracy and the above decomposition can be restricted to the block of $\mathrm{cov}(P)$ of the parameters $f, d, m, e_u, e_v, \Phi, \Psi$, yielding only 7 sets of independent parameter errors $\Delta P_1, \Delta P_2, ..., \Delta P_7$.

D. Reconstruction Accuracy

The reconstruction accuracy is evaluated for both loss of spatial resolution and deformation of the reconstructed images by simulating the reconstruction of a grid of point sources. Relatively simple grids can be used, since the circular orbit

of the pinhole camera causes circular symmetry of the reconstruction properties, with respect to the axis of rotation. (In practice, the grid of 11 coplanar point sources, shown in figure 3, will be used.)

Consider the reconstruction of a point source (x_k, y_k, z_k) from its pinhole projections $(u_k(\theta), v_k(\theta))$ at the projection angles θ. If it is reconstructed using the correct acquisition geometry $f, d, m, e_u, e_v, \Phi, \Psi$, all projection rays

$$\begin{aligned} & fx''' + (u_k(\theta) - m\cos\Psi - e_u)y''' + \\ & \quad d(u_k(\theta) - m\cos\Psi - e_u) - fm\cos\Psi = 0 \\ & fz''' + (v_k(\theta) - m\sin\Psi - e_v)y''' + \\ & \quad d(v_k(\theta) - m\sin\Psi - e_v) - fm\sin\Psi = 0 \end{aligned} \quad (18)$$

intersect at the correct point (x_k, y_k, z_k) in the field of view. Mathematically, the above projection rays yield a set of linear equations

$$\begin{aligned} a_{uk}(\theta)x + b_{uk}(\theta)y + c_{uk}(\theta)z + d_{uk}(\theta) = 0 \quad \forall\theta \\ a_{vk}(\theta)x + b_{vk}(\theta)y + c_{vk}(\theta)z + d_{vk}(\theta) = 0 \quad \forall\theta \end{aligned}$$

or

$$A_k X + B_k = 0 \quad (19)$$

with the unique solution $X_k = [x_k, y_k, z_k]^T$. For an incorrect acquisition geometry $f', d', m', e'_u, e'_v, \Phi', \Psi'$, a similar set of equations exists, but the system will generally be overdetermined. We assume that in this case, the point source will be reconstructed at the least squares solution

$$X_k^R = -\left(A_k^T A_k\right)^{-1} A_k^T B_k \quad (20)$$

of this linear system.

The distances $S_k(\theta)$ from the 'reconstructed' point source $X_k^R = [x_k^R, y_k^R, z_k^R]^T$ to its different projection rays, provide a measure of the loss in spatial resolution due to the incorrect calibration results. These distances can be specified as vectors $S_k = [s_{xk}, s_{yk}, s_{zk}]^T$ in the xyz coordinate system with a specific length and direction. The loss in spatial resolution is specified in turn as the length of the largest vector for all point sources and projection angles, regardless of its direction

$$\text{res. loss} = \max_\theta(\max_k(\|S_k(\theta)\|)) \quad (21)$$

in which $\|.\|$ denotes the L_2 norm of a vector.

The image deformation due to the incorrect acquisition geometry is further evaluated by considering the displacement vectors $L_k = [l_{xk}, l_{yk}, l_{zk}]^T = [|x_k^R - x_k|, |y_k^R - y_k|, |z_k^R - z_k|]^T$ of the reconstructed point sources with respect to their original locations. These vectors are first corrected for a global translation and a global rotation of all 11 point sources along and around the axis of rotation. The remaining displacements reflect the deformation of the reconstructed image (with respect to the original phantom). This image deformation will be specified as the largest displacement of all the point sources, regardless of its direction

$$\text{img. deform.} = \max_k(\|L_k\|). \quad (22)$$

The decomposition of a covariance matrix $\text{cov}(P) = \Gamma\Gamma^T$, explained in the previous section, yields seven sets of independent parameter estimate errors $\Delta P_1, \Delta P_2, ..., \Delta P_7$. In such a case, the distances $\|S_{kPj}(\theta)\|$ and $\|L_{kPj}\|$, obtained with those 7 sets, are first quadratically added together, before evaluating (21) and (22).

$$\|S_k(\theta)\| = \sqrt{\sum_j \|S_{kPj}(\theta)\|^2} \quad (23)$$

$$\|L_k\| = \sqrt{\sum_j \|T_{kPj}\|^2} \quad (24)$$

This approach is based on the assumption that the 7 sets of errors each have an independent effect on the image reconstruction accuracy.

III. Experiments

A. Optimal Calibration Setup

The first experiment evaluates the effect of the calibration setup on the estimation and reconstruction accuracy, both in the case of noisy calibration data and the case of phantom model errors. The aim is to find a calibration setup for optimal reconstruction accuracy, and possibly also optimal estimation accuracy, in practice. For this purpose, the estimation and reconstruction accuracy are calculated, as described in section II, for a large set of calibration setups. The setups are generated by systematically varying the positions of the 3 calibration point sources over a spherical grid of possible point source locations in the pinhole field of view. A cross section of the grid is shown in figure 2, and the complete grid is obtained by rotating this cross section over 0, 45, 90 and 135 degree about the axis of rotation. We assume that the set of calibration setups obtained in this way, is sufficiently representative for the actual (infinite) set of possible calibration setups. Appendix II further demonstrates that the spherical volume of the point source grid covers almost the entire field of view for pinhole cameras with small to moderate acceptance angles. The pinhole field of view is here defined as that part of space which is seen by the camera at all projection angles. The results are inspected for the smallest possible image deformations and resolution losses, and also for the lowest standard deviations of the parameter estimates.

The experiment is performed for a pinhole camera with 24 cm focal length f. The focal point is rotating at 4 cm distance d around the rotation axis and the pinhole collimator has a 60 degree acceptance angle α. The parameters m, e_u, e_v, Φ and Ψ are all equal to zero, simulating an 'ideal' pinhole system. This acquisition geometry yields a field of view of 4 cm in diameter and 64 equidistant projections over 360 degree are simulated. The noise on the calibration data U is modeled by a diagonal covariance matrix cov(U) in (14) with (independent) variances of $0.09\ \text{mm}^2$ (0.3 mm standard deviation) for each coordinate of U. This noise is visually worse than the noise of real calibration measurements with the above acquisition geometry. The phantom model errors are also represented by a diagonal covariance matrix cov(X) (16), with (independent) variances of $0.01\ \text{mm}^2$ (0.1 mm standard deviation) for each Cartesian coordinate of X. Finally, the point source grid, used to evaluate the reconstruction accuracy is shown in Figure 3.

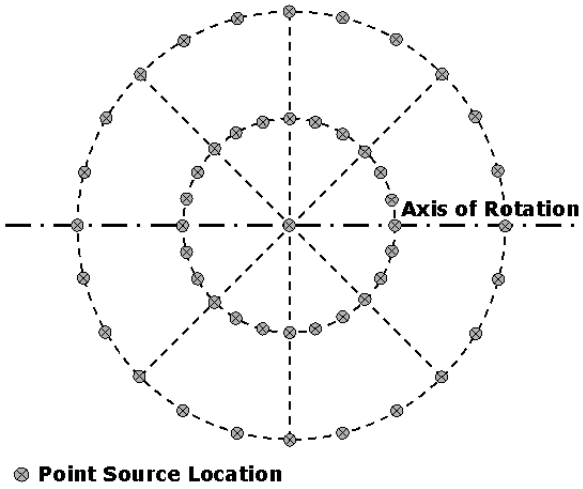

Fig. 2. Cross section of the spherical grid of possible point source locations in the field of view of the pinhole camera. The complete grid is obtained by rotating the displayed grid over 0, 45, 90 and 135 degree about the axis of rotation.

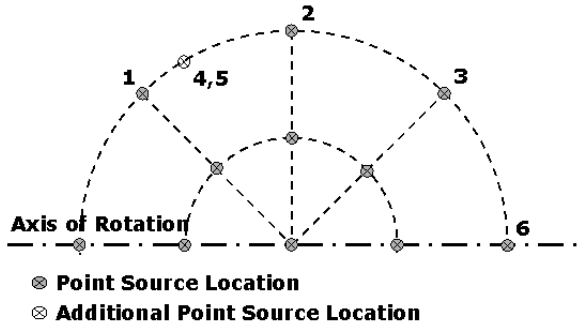

Fig. 3. Grid of point sources to evaluate the deformation of reconstructed images. The numbers 1,2,3 and 4,5,6 indicate a relationship with the calibration point sources in Figure 4. The additional point source 4,5 is only used in experiment III.C for the optimal calibration setup 'opt2'.

B. Linear System Verification

In this experiment, the validity of the linear systems (12) and (15) are evaluated for the optimal calibration setups of the first experiment. This is done by applying the calibration method to a series of simulated calibration measurements. First, the noiseless projection locations U_0 of the calibration point sources are calculated with (1) and (2) for the correct calibration setup X. Next, 250 random noise realizations of either the projection data U_0 (Gaussian noise, 0.3 mm standard deviation) or the calibration setup X (Gaussian noise, 0.1 mm standard deviation) are generated. To evaluate the case of noisy calibration data, the calibration method is directly applied to each of the 250 noise realizations of U_0. For the phantom errors case, the noise realizations of X are used to calculate incorrect phantom models $d'_{12}, d'_{13}, d'_{23}$, which are then used in calibration calculations with the noiseless calibration data U_0. In the combined case, 250 different noise realizations of both U_0 and X are finally generated to simulate 250 calibrations with noise on the data and phantom model errors. In each of the cases, mean values, variances and covariances of the parameter estimates are calculated and compared with the corresponding results of the linear system approaches.

The experiment is conducted for the same pinhole and acquisition characteristics as in the first experiment.

C. Image Deformation

In the previous experiment, random modifications ΔX of the optimal calibration setups were generated by modifying the Cartesian coordinates X of the calibration point sources $i = 1, 2, 3$. For each calibration point source i individually, this modification causes a displacement of the point source, represented by the vector ΔX_i. In the evaluation of the reconstruction accuracy, the displacements L_k of the point sources k of the point source grid of figure 3 are studied. Keeping in mind the circular symmetry of the reconstruction properties, each of the calibration point sources i can be thought to be located at a specific location in the grid of point sources k, as indicated in the figures 3 and 4 (see further) by the corresponding numbers. With the displacements ΔX_i already calculated in the previous experiment, this additional experiment studies their relation with the resulting displacements $L_{k=i}$ of the corresponding point sources after reconstruction. It does so for both optimal calibration setups and is performed for the situation in which only phantom model errors are present. The results ΔP of each of the 250 calibrations of the previous experiment are used to evaluate the reconstruction accuracy as described in section II.D and the resulting displacements $\|L_{k=i}\|$ are compared with the original displacements $\|\Delta X_i\|$ of the corresponding point sources. Note that, for calibration setup 'opt2', an additional point source '$4, 5$' was added to the grid of figure 3 to enable this experiment.

The experiment is again conducted for the same pinhole and acquisition characteristics as in the first experiment.

IV. Results

A. Optimal Calibration Setup

With the standard deviations of the 7 acquisition parameters $f, d, m, e_u, e_v, \Phi, \Psi$ expressing the estimation accuracy, and with the resolution loss (21) and image deformation (22) expressing the reconstruction accuracy, a total of 9 parameters $p_i \quad i = 1, 9$ express the accuracy of the entire calibration-reconstruction process. For the same calibration setup, the accuracies p_i generally differ in the different situations of noisy data, phantom model errors and the combination of both. In each situation, different calibration setups further minimize different parameters p_i, yielding p_i^{min}. No solution was found minimizing all 9 parameters p_i simultaneously in either a single or all 3 cases.

For the case of noisy calibration data, a large number of setups can be found, yielding maximum image deformation and maximum loss of spatial resolution of less than 0.05 mm, while the attainable image resolution is expected to be 0.5 mm or worse. As these errors are much smaller than the attainable resolution, each of these setups can be considered to be equally favorable. In the phantom model errors case, also a large number of setups can be found yielding losses in spatial resolution of less than 0.05 mm, but image deformation is 0.20 mm or higher for all possible calibration setups. Nevertheless,

a relatively large number of setups can be found with image deformations of less than 0.25 mm. Finally, roughly the same amount of setups satisfy these criteria in both cases

$$\begin{aligned} \text{res. loss} &\leq 0.05 \text{ mm} && \text{for noisy data} && (25)\\ \text{img. deform.} &\leq 0.05 \text{ mm} && && (26)\\ \text{res. loss} &\leq 0.05 \text{ mm} && \text{for model errors.} && (27)\\ \text{img. deform.} &\leq 0.25 \text{ mm} && && (28) \end{aligned}$$

This indicates that the optimality of the calibration setups in terms of the reconstruction accuracy is not very clearly defined and many calibration setups can in this respect be found to be optimal.

This relative abundance of calibration setups with excellent reconstruction accuracy in any situation, is exploited to find solutions which also yield good estimation accuracy. The calibration setups 'opt1' and 'opt2' nearly minimize all 9 parameters p_i simultaneously in the noisy data and the phantom model errors case respectively. More precisely, they minimize the objective

$$\sqrt{\sum_{i=1}^{9} (p_i - p_i^{min})^2} \tag{29}$$

in those respective cases (with the parameters p_i expressed in millimeters or degrees), while also satisfying the reconstruction accuracy conditions (25) to (28). The setups are shown in figure 4 and table III lists the parameters p_i together with the minimum values p_i^{min} for each case. Note that the minimum values p_i^{min} are generally obtained with different calibration setups. Both optimal setups consist of a triangular phantom configuration with the axis of rotation in the plane of the triangle and all 3 point sources on the edge of the (spherical) field of view. In 'opt1' the triangle is isosceles, with the third side parallel to the axis of rotation. In 'opt2' the triangle is equilateral and one point source is located on the axis of rotation.

Figure 5 and 6 illustrate the 6 calibration setups with the best performance in terms of the objective (29) for the noisy data and phantom model errors case respectively and satisfying the restrictions (25) to (28) (in both cases). In comparison with the calibration setups (a), the setups (b) to (f) yield only a marginal increase in the value of the objective (29), indicating that this cost is relatively flat and that multiple effective optima are actually available.

Regardless of the situation in which they were tested, the optimal calibration setups 'opt1' and 'opt2' only show small deviations from the optimal accuracy. In terms of reconstruction accuracy, the differences are so small that they will not be noticeable in practice. In the phantom model errors and combined cases, the calibration setup 'opt1' shows a marked increase in the standard deviation of the focal length f and small increases in the standard deviations of e_v and Φ. The calibration setup 'opt2' on the other hand, shows small increases in the standard deviations of f, d, e_v and Φ in the case of noisy calibration data and in the combined case.

The image deformations (0.215 mm and 0.202 mm) of the optimal setups in the phantom error case are clearly smaller than the 0.346 mm root mean square value of the

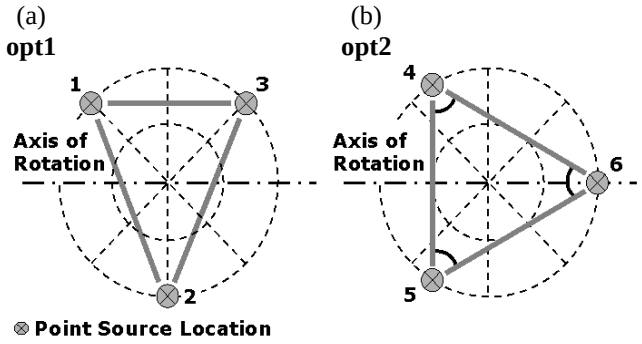

Fig. 4. Optimal Calibration Setups: (a) 'opt1' and (b) 'opt2'. The numbers 1,2,3 and 4,5,6 indicate a relationship of the calibration point sources with specific point sources of the point source grid of Figure (3).

displacements $2||\Delta X_i||$ causing them. (Twice the value of $||\Delta X_i||$ is selected, since the errors ΔP were calculated from two standard deviations of the geometric parameter estimates.) The image deformation due to an incorrect phantom model will thereby generally be of the same magnitude or less than the deformation of the phantom model itself.

B. Linear System Verification

The results of the calibration simulations are indicated by 'sim1' and 'sim2' for the calibration setups 'opt1' and 'opt2' respectively. The standard deviations of the parameters estimates, presented table III, show excellent agreement between the linear system and simulation approaches. The correlations between the estimates of the different parameter estimates, shown in table IV, further show good agreement as well between the different approaches. (Note that the cross correlations for parameters with zero variance are omitted in table IV). Finally, the linear system approaches assume zero bias on the parameter estimate results. Table V lists the mean values of the different parameter estimates. Considering the standard deviations for these parameter estimates, the mean values are always very close to the correct values, confirming the validity of the zero bias implicit assumption of the linear systems.

C. Image Deformation

In figure 7, the displacements $||L_i||$ of the reconstructed point sources $1, 2, 3$ and $4, 5, 6$ of figure 3 are plotted against the initial displacements ΔX_i of the corresponding point sources of the calibration setups 'opt1' and 'opt2' respectively. The reconstruction image deformations $||L_i||$ are generally smaller than the modeling errors $||\Delta X_i||$ for both calibration setups and for each of its point sources. The sum of the displacements $||L_i||$ of the point source reconstructions $1, 2, 3$ or $4, 5, 6$ is further always less than the sum of the corresponding modeling errors $||\Delta X_i||$. These data again support the earlier observation that the reconstruction image deformation due to an incorrect phantom model is of the same magnitude or less than the deformation of the phantom model itself.

TABLE III

		Reconstruction Accuracy		Estimation Accuracy (Standard deviation)						
		img. deform. [mm]	res. loss [mm]	f [mm]	d [mm]	m [mm]	e_u [mm]	e_v [mm]	Φ [deg]	Ψ [deg]
Data Noise	min	0.013	0.024	0.20	0.03	0.03	0.22	0.19	0.04	0.01
	opt1	0.014	0.025	0.21	0.03	0.03	0.23	0.19	0.04	0.01
	sim1			0.22	0.03	0.03	0.23	0.20	0.04	0.01
	opt2	0.018	0.034	0.35	0.05	0.03	0.23	0.29	0.05	0.01
	sim2			0.35	0.05	0.03	0.23	0.31	0.05	0.01
Model Errors	min	0.201	0.002	0.00	0.12	0.00	0.00	2.77	0.66	0.00
	opt1	0.215	0.027	0.54	0.13	0.00	0.00	2.95	0.71	0.00
	sim1			0.53	0.13	0.00	0.02	2.93	0.70	0.00
	opt2	0.202	0.002	0.00	0.12	0.00	0.00	2.77	0.66	0.00
	sim2			0.05	0.11	0.00	0.01	2.63	0.63	0.00
Combination	min	0.202	0.025	0.20	0.12	0.03	0.22	2.78	0.66	0.01
	opt1	0.215	0.037	0.58	0.13	0.03	0.23	2.95	0.71	0.01
	sim1			0.58	0.13	0.03	0.23	2.95	0.71	0.01
	opt2	0.203	0.034	0.35	0.13	0.03	0.23	2.79	0.66	0.01
	sim2			0.33	0.13	0.03	0.24	2.76	0.66	0.01

TABLE IV

PARAMETER ESTIMATE CROSS CORRELATIONS

		f	d	m	e_u	e_v	Φ	Ψ		f	d	m	e_u	e_v	Φ	Ψ
Data Noise	f	**1.00**	**0.97**	0.00	0.00	0.00	0.00	0.00	f	**1.00**	**0.99**	0.00	0.00	**0.70**	**0.52**	0.00
	d		**1.00**	0.00	0.00	0.00	0.00	0.00	d		**1.00**	0.00	0.00	**0.71**	**0.51**	0.00
	m			**1.00**	**-1.00**	0.00	0.00	0.00	m			**1.00**	**-1.00**	0.00	0.00	0.03
	e_u				**1.00**	0.00	0.00	0.00	e_u				**1.00**	0.00	0.00	0.03
	e_v		**opt1**			**1.00**	**0.92**	0.00	e_v		**opt2**			**1.00**	**0.92**	0.00
	Φ						**1.00**	0.00	Φ						**1.00**	0.00
	Ψ							**1.00**	Ψ							**1.00**
		f	d	m	e_u	e_v	Φ	Ψ		f	d	m	e_u	e_v	Φ	Ψ
	f	**1.00**	**0.97**	-0.06	0.06	-0.08	-0.12	-0.06	f	**1.00**	**0.99**	-0.07	0.07	**0.69**	**0.52**	-0.18
	d		**1.00**	-0.04	0.05	-0.08	-0.13	-0.07	d		**1.00**	-0.07	0.07	**0.70**	**0.51**	-0.17
	m			**1.00**	**-1.00**	0.02	-0.01	-0.09	m			**1.00**	**-1.00**	-0.03	-0.05	-0.07
	e_u				**1.00**	-0.03	0.00	-0.09	e_u				**1.00**	0.03	0.05	0.08
	e_v		**sim1**			**1.00**	**0.91**	0.00	e_v		**sim2**			**1.00**	**0.93**	-0.02
	Φ						**1.00**	0.06	Φ						**1.00**	0.00
	Ψ							**1.00**	Ψ							**1.00**
Model Errors		f	d	m	e_u	e_v	Φ	Ψ		f	d	m	e_u	e_v	Φ	Ψ
	f	**1.00**	0.43			0.00	0.00		f	**1.00**						
	d		**1.00**			0.00	0.00		d		**1.00**			0.00	0.00	
	m			**1.00**					m			**1.00**				
	e_u				**1.00**				e_u				**1.00**			
	e_v		**opt1**			**1.00**	**1.00**		e_v		**opt2**			**1.00**	**1.00**	
	Φ						**1.00**		Φ						**1.00**	
	Ψ							**1.00**	Ψ							**1.00**
		f	d	m	e_u	e_v	Φ	Ψ		f	d	m	e_u	e_v	Φ	Ψ
	f	**1.00**	0.43			-0.08	-0.08		f	**1.00**						
	d		**1.00**			-0.09	-0.09		d		**1.00**			0.14	0.14	
	m			**1.00**					m			**1.00**				
	e_u				**1.00**				e_u				**1.00**			
	e_v		**sim1**			**1.00**	**1.00**		e_v		**sim2**			**1.00**	**1.00**	
	Φ						**1.00**		Φ						**1.00**	
	Ψ							**1.00**	Ψ							**1.00**
Combi-nation		f	d	m	e_u	e_v	Φ	Ψ		f	d	m	e_u	e_v	Φ	Ψ
	f	**1.00**	**0.47**	0.00	0.00	0.00	0.00	0.00	f	**1.00**	**0.41**	0.00	0.00	0.07	0.04	0.00
	d		**1.00**	0.00	0.00	0.00	0.00	0.00	d		**1.00**	0.00	0.00	0.03	0.02	0.00
	m			**1.00**	**-1.00**	0.00	0.00	0.00	m			**1.00**	**-1.00**	0.00	0.00	0.03
	e_u				**1.00**	0.00	0.00	0.00	e_u				**1.00**	0.00	0.00	-0.03
	e_v		**opt1**			**1.00**	**1.00**	0.00	e_v		**opt2**			**1.00**	**1.00**	0.00
	Φ						**1.00**	0.00	Φ						**1.00**	0.00
	Ψ							**1.00**	Ψ							**1.00**
		f	d	m	e_u	e_v	Φ	Ψ		f	d	m	e_u	e_v	Φ	Ψ
	f	**1.00**	**0.49**	-0.06	0.05	0.00	0.00	0.05	f	**1.00**	**0.42**	0.05	-0.05	0.07	0.04	0.09
	d		**1.00**	-0.08	0.09	0.03	0.03	0.03	d		**1.00**	0.06	-0.06	0.07	0.06	-0.01
	m			**1.00**	**-1.00**	0.05	0.05	0.00	m			**1.00**	**-1.00**	-0.01	-0.01	-0.04
	e_u				**1.00**	-0.05	-0.06	0.01	e_u				**1.00**	0.02	0.02	0.04
	e_v		**sim1**			**1.00**	**1.00**	-0.12	e_v		**sim2**			**1.00**	**1.00**	-0.01
	Φ						**1.00**	-0.13	Φ						**1.00**	-0.01
	Ψ							**1.00**	Ψ							**1.00**

Cross correlations for parameters with zero standard deviation are omitted.

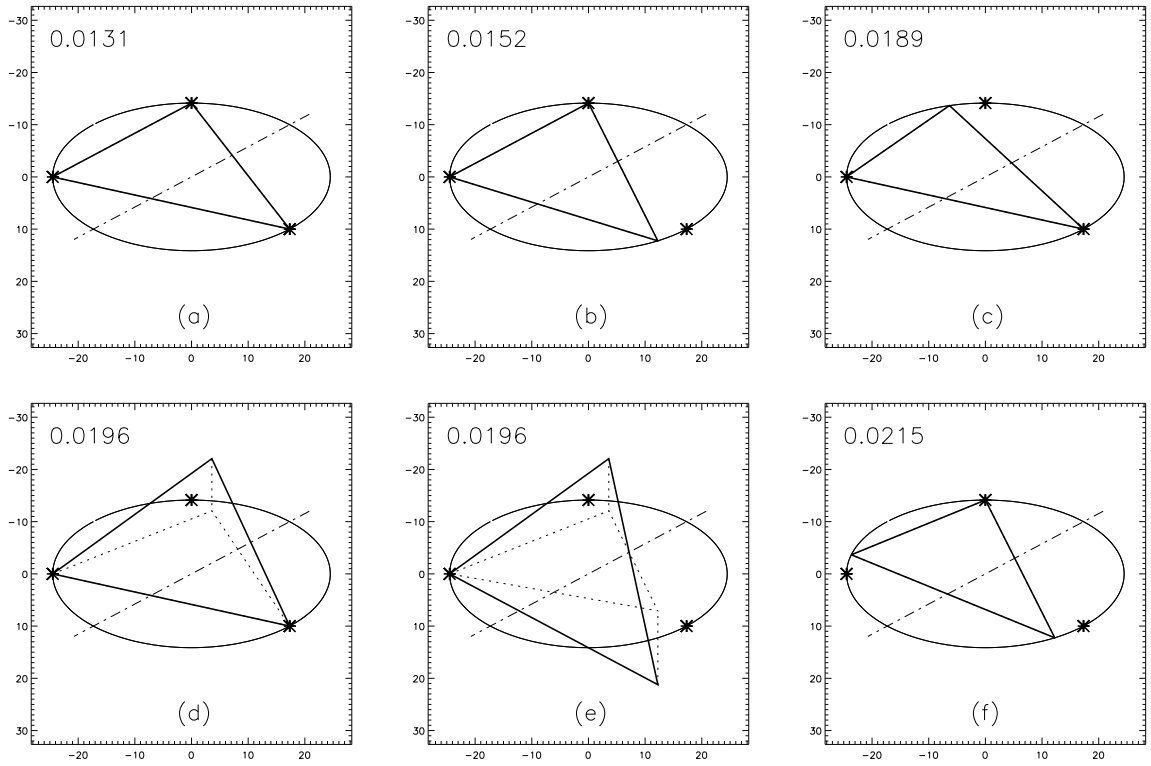

Fig. 5. The 6 calibration setups with the best performance in terms of the objective (29) for noisy calibration data. The value of objective (29) is indicated in the figure. The circle represents the intersection of the horizontal plane containing the axis of rotation (the dash-dotted line) with the pinhole field of view. Asterisks indicate the position of the point sources of 'opt1'. The solid triangles show the calibration setups in 3D, while the dotted triangles are the orthogonal projections of these calibration setups on the horizontal plane.

TABLE V

		Estimation Accuracy (Mean value)						
		f [mm]	d [mm]	m [mm]	e_u [mm]	e_v [mm]	Φ [deg]	Ψ [deg]
Exact	opt	240.00	40.00	0.00	0.00	0.00	0.00	0.00
Data Noise	sim1	239.99	40.00	0.00	0.01	0.00	0.00	0.00
	sim2	240.01	40.00	0.00	0.03	0.03	0.01	0.00
Model Errors	sim1	239.96	40.01	0.00	0.00	-0.13	-0.03	0.00
	sim2	240.01	40.01	0.00	0.00	0.32	0.07	0.00
Combination	sim1	239.96	40.00	0.00	-0.02	0.32	0.08	0.00
	sim2	240.03	40.01	0.00	-0.01	0.14	0.03	0.00

V. Discussion

The method we developed to determine the acquisition geometry of a pinhole camera [1], is based on the assumption that the calibration phantom is the representation of an image, which can be thought of as an infinite collection of point sources. Stated in this way, the best calibration phantom, is the one best representing the entire image. From this point of view, the best way to improve the phantom probably consists in adding additional point sources to it. It also suggests that the point sources should be distributed to cover the entire field of view, although not necessarily in a uniform way. Our results indicate that the theoretically minimal number of point sources [1], placed at well chosen locations in the field of view, is already sufficient for practical purposes. The above concept also explains how the use of an incorrect phantom model, results in an equivalent deformation of the reconstructed image. The calibration minimizes the inconsistency between the fixed, but incorrect phantom model and the measured projections by modifying the projector. During reconstruction, the same projector is then used to generate an image, which is consistent with its projections.

The optimal calibration setups seem to agree with earlier findings of Wang $et\ al.$ [4] and Noo $et\ al.$ [6] about optimal setups for their calibration methods. Wang $et\ al.$ [4] used a single calibration point source and reported that the estimation accuracy improved with larger distances between the point source and the axis of rotation. On the other hand, Noo $et\ al.$ [6] used two point sources and reported that these point sources should be placed well apart from each other and from the focal plane, with the focal plane being the plane in which the focal point is rotating during image acquisition. In both optimal calibration setups, the point sources are all located on the edge of the field of view, yielding the best compromise in

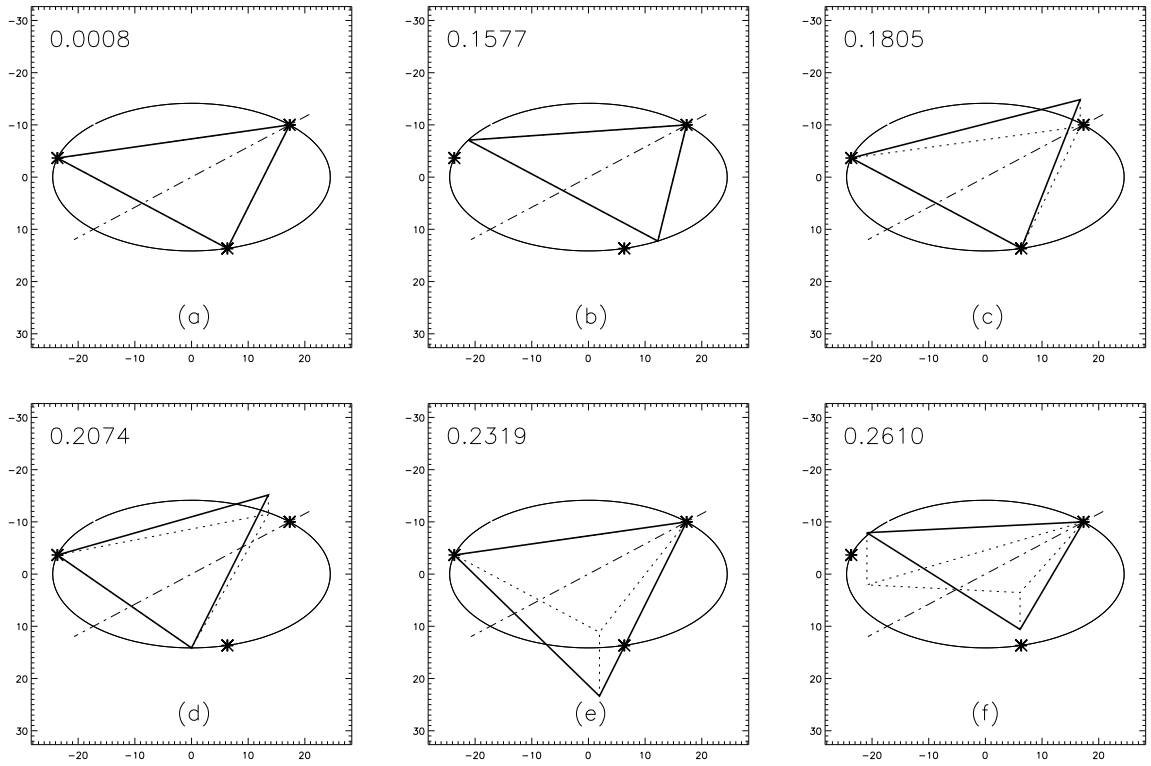

Fig. 6. The 6 calibration setups with the best performance in terms of the objective (29) for phantom model errors. The value of objective (29) is indicated in the figure. The circle represents the intersection of the horizontal plane containing the axis of rotation (the dash-dotted line) with the pinhole field of view. Asterisks indicate the position of the point sources of 'opt2'. The solid triangles show the calibration setups in 3D, while the dotted triangles are the orthogonal projections of these calibration setups on the horizontal plane.

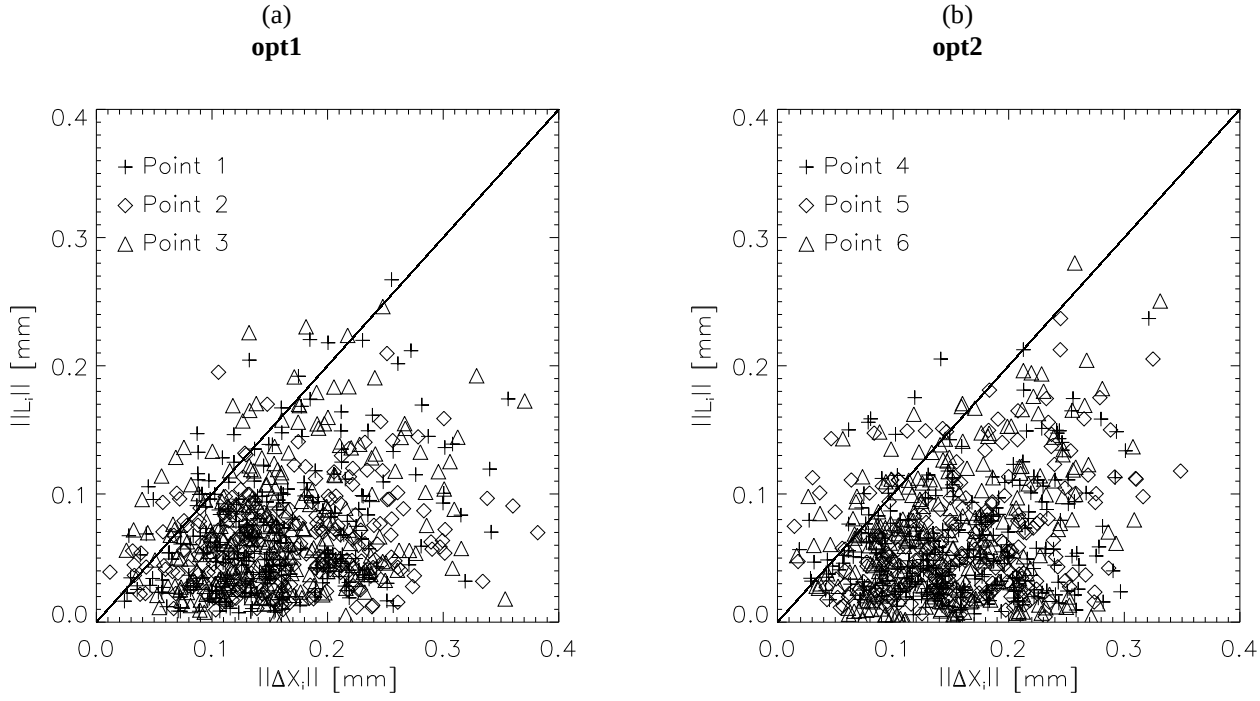

Fig. 7. Displacements $||L_i||$ of the reconstructed point sources versus the displacements $||\Delta X_i||$ of the calibration model with respect to the phantom configuration. (a) results for 'opt1' and (b) results for 'opt2'.

distance to the axis of rotation and distance to the focal plane for a spherical field of view. In calibration setup 'opt1', point source 2 is located exactly in the focal plane, but at the largest possible distance from the rotation axis. The point sources 1 and 3 on the other hand, are located at a considerable distance from the focal plane, but without sacrificing too much of their distance to the rotation axis. In the calibration setup 'opt2', point source 6 is placed as far as possible from the focal plane and therefore on the axis of rotation. Point sources 4 and 5 are placed at a considerable distance from the axis of rotation, but now closer to the focal plane. Some types of calibration setups are also specifically prohibited by theory [1]. The 3 point sources each must have a different position, they may not all 3 have the same z coordinate and at least one point source must be located off the axis of rotation. As expected, the optimal calibration setups are clearly different from these forbidden setups.

In practice, noise on the calibration data and errors on the phantom model will always be present in calibration experiments. In theory, the optimal setup for each particular calibration may depend on the relative magnitude of the noise and the model errors. The calibration setups we propose, are however nearly optimal for both noise and model errors, which suggests that their performance is rather independent of this relative magnitude. Further, for the realistic noise level of the experiments, the small phantom model errors (0.1 mm standard deviation) clearly dominate the reconstruction accuracy. Note however, that for a fixed phantom configuration, the phantom model (distances between the point sources) only needs to be measured once. Consequently, this should be done with care to keep the errors below the maximum tolerable deformations of reconstructed images. The inaccuracies due to noise, on the other hand, only have a very limited impact on the reconstruction accuracy with the proposed calibration setups and further noise reduction does not seem necessary.

Apart from being quite simple and ignoring the difference between millimeters and degrees, one can argue that the objective (29) used to find the optimal calibration setups 'opt1' and 'opt2' is rather arbitrary. The main conclusion of section IV.A is however that the geometrically attractive setups 'opt1' and 'opt2' yield nearly the best possible accuracies of all parameters p_i, especially with respect to the reconstruction accuracy, and they do so in all situations studied. Although the objective (29) may be simple, it will penalize calibration setups with a markedly different behavior. Further, other setups closely resembling 'opt1' and 'opt2' yield very similar accuracies in terms of the above objective (see figure 5 and 6), suggesting that the overall accuracy related to the proposed setups is stable as well.

The approach of the first experiment to start with a linear system to calculate the calibration covariance matrix cov(P) and then decompose it into a set of independent errors $\Delta P_1, ..., \Delta P_7$ to evaluate the reconstruction accuracy, may seem cumbersome. Two possible solutions have been considered. A first solution might be to perform a series of calibration simulations with noisy data sets (ΔU) to calculate the estimation accuracy. The result ΔP of each simulation individually can then be used to evaluate the reconstruction accuracy ΔP for that particular noise realization ΔU, while the calibration covariance matrix cov(P) can still be calculated from a sufficiently large number of simulations, like in the second and third experiment. Unfortunately, this procedure has to be repeated for each calibration setup and is far too slow for such purposes. A second possibility is the use of some linear system to evaluate the reconstruction accuracy directly from the covariance matrix cov(P), avoiding its decomposition. However, the reconstruction accuracy must be evaluated for both image deformation and spatial resolution. Further, a global rotation and translation of the reconstructed image should not be considered as image deformations. No linear system has been found that satisfies these requirements.

VI. Conclusion

Two specific configurations of three point sources with a specific position and orientation in the field of view have been proposed as optimal pinhole SPECT calibration setups in practice. The setups yield optimal reconstruction accuracy, while the accuracy of the estimated pinhole acquisition geometry is nearly optimal as well. With the proposed calibration setups, errors in the phantom model will cause image deformations of the same magnitude or less.

Appendix I
Covariance Matrix Decomposition

This section demonstrates a recursive method to calculate the matrix Γ of (15) for a small 3x3 covariance matrix

$$\mathrm{cov}(P) = \begin{bmatrix} \sigma_{xx} & \sigma_{xy} & \sigma_{xz} \\ \sigma_{xy} & \sigma_{yy} & \sigma_{yz} \\ \sigma_{xz} & \sigma_{yz} & \sigma_{zz} \end{bmatrix}. \tag{30}$$

The first column of Γ, which equals $\frac{\Delta P_1}{2}$, is calculated as

$$\frac{\Delta P_1}{2} = \begin{bmatrix} \sqrt{\sigma_{xx}} \\ \alpha\sqrt{\sigma_{xx}} \\ \beta\sqrt{\sigma_{xx}} \end{bmatrix} \tag{31}$$

with

$$\alpha = \frac{\sigma_{xy}}{\sigma_{xx}} \tag{32}$$

$$\beta = \frac{\sigma_{xz}}{\sigma_{xx}} \tag{33}$$

and cov(P) is modified into cov($P1$)

$$\mathrm{cov}(P_1) = \begin{bmatrix} 0 & 0 & 0 \\ 0 & \sigma_{yy} - \alpha^2\sigma_{xx} & \sigma_{yz} - \alpha\beta\sigma_{xx} \\ 0 & \sigma_{yz} - \alpha\beta\sigma_{xx} & \sigma_{zz} - \beta^2\sigma_{xx} \end{bmatrix}. \tag{34}$$

In this new covariance matrix cov(P_1), the variance of x has been eliminated and the variances of y and z have been reduced by the appropriate amount, according to their covariances with the parameter x. The covariance σ_{yz} has also been adapted to the new values of the variances of y and z. The above procedure is now systematically repeated for the other diagonal elements, yielding the other columns of Γ. For

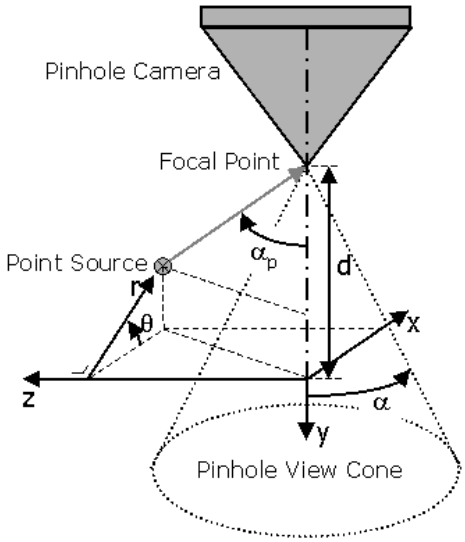

Fig. 8. Point source rotating in front of a stationary pinhole camera.

the above 3x3 matrix this procedure yields

$$\Gamma = \begin{bmatrix} \sqrt{\sigma_{xx}} & 0 & 0 \\ \alpha\sqrt{\sigma_{xx}} & \sqrt{\sigma_{yy} - \alpha^2\sigma_{xx}} & 0 \\ \beta\sqrt{\sigma_{xx}} & \gamma\sqrt{\sigma_{yy} - \alpha^2\sigma_{xx}} & \sqrt{\begin{array}{c}\sigma_{zz} - \gamma^2\sigma_{yy} + \\ (\alpha^2\gamma^2 - \beta^2)\sigma_{xx}\end{array}} \end{bmatrix}. \quad (35)$$

and with

$$\gamma = \frac{\sigma_{yz} - \alpha\beta\sigma_{xx}}{\sigma_{yy} - \alpha^2\sigma_{xx}}. \quad (36)$$

From (35), it is easy to proof that $\text{cov}(P) = \Gamma\Gamma^T$ (17) and extension of the method to larger covariance matrices is straightforward.

APPENDIX II
PINHOLE SPECT FIELD OF VIEW

This appendix calculates the shape of the field of view of a pinhole camera with a circular detector orbit and the overlap with the largest sphere inscribed in this field of view. The results are valid for zero mechanical offset m and zero tilt angle Φ.

Consider a point source rotating around an axis at a distance d in front of a stationary pinhole camera, as shown in Figure 8. During rotation, the point source describes a circle with radius r in a plane at a distance z from the central ray of the pinhole camera. At each position θ, the point source projection ray intersects the central ray at an angle α_p

$$\alpha_p = \arctan\left(\frac{\sqrt{r^2\cos^2\theta + z^2}}{d - r\sin\theta}\right). \quad (37)$$

To be located in the field of view, the ray angle α_p of the point source projection must be less than half of the acceptance angle of the pinhole aperture, represented by α. At each z-location, the maximum radius r is thereby limited. During rotation, the angle α_p maximizes to

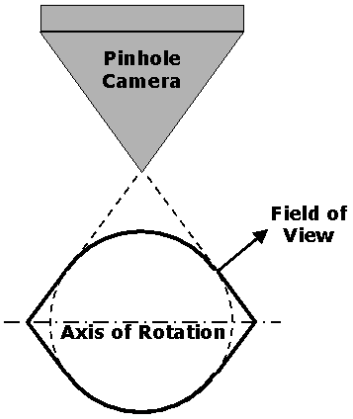

Fig. 9. Pinhole SPECT Field of View.

$$\alpha_{p,max} = \arctan\left(\frac{z}{d \pm r}\right) \quad \text{if } r^2 + z^2 \geq rd \quad (38)$$

$$\alpha_{p,max} = \arctan\left(\sqrt{\frac{r^2+z^2}{d^2-r^2-z^2}}\right) \quad \text{if } r^2 + z^2 < rd. \quad (39)$$

At this maximum angle position of the point source $\alpha_{p,max}$, the radius of rotation r_{max} that yields $\alpha_{p,max} = \alpha$ can be calculated

$$r_{max} = d - \frac{z}{\tan\alpha} \quad \text{if } z \geq d\sin\alpha\cos\alpha \quad (40)$$

$$r_{max} = \sqrt{d^2\sin^2\alpha - z^2} \quad \text{if } z < d\sin\alpha\cos\alpha. \quad (41)$$

Figure 9 illustrates the shape of this field of view. The field of view consists of a central spherical zone ($z < d\sin\alpha\cos\alpha$) with two conical extensions along the rotation axis ($z \geq d\sin\alpha\cos\alpha$). From this observation, it is easy to calculate the volume V_{fov} of this field of view.

$$V_{fov} = \frac{4}{3}\pi d^3\sin^3\alpha\ \frac{\cos^2\alpha + 1}{2\,cos\alpha}. \quad (42)$$

Further, it is obvious from (40,41) that the largest sphere that can be inscribed in this field of view, is a sphere with radius $d\sin\alpha$ located at the center of the field of view. The volume V_{sphere} is readily calculated as

$$V_{sphere} = \frac{4}{3}\pi d^3\sin^3\alpha. \quad (43)$$

The overlap between this sphere and the actual field of view only depends on the aperture angle 2α of the pinhole system.

$$\frac{V_{sphere}}{V_{fov}} = \frac{2\,cos\alpha}{\cos^2\alpha + 1}. \quad (44)$$

Figure 10 shows the overlap of the sphere and the actual field of view. For small to moderate aperture angles, the sphere covers almost the entire field of view.

REFERENCES

[1] D. Bequé, J. Nuyts, G. Bormans, P. Suetens, and P. Dupont, "Characterization of Pinhole SPECT Acquisition Geometry, " *IEEE Trans. Med. Imag.*, Vol. 22, No. 5, pp. 599-612.

[2] G. T. Gullberg, B. M. W. Tsui, C. R. Crawford, J. G. Ballard, and J. T. Hagius, "Estimation of geometrical parameters and collimator evaluation for cone beam tomography," *Med. Phys.*, vol. 17(2), pp. 264–272, 1990.

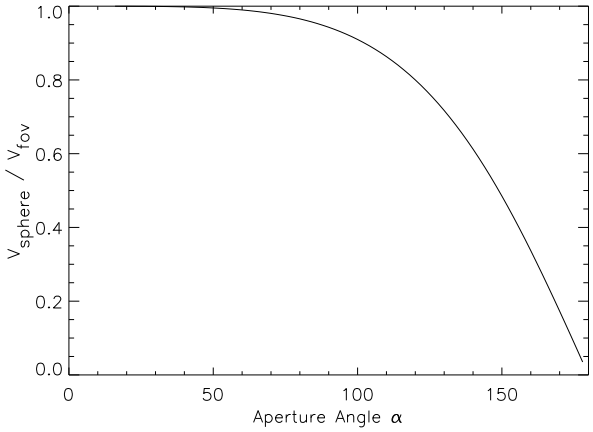

Fig. 10. Fractional overlap of a spherical approximation (V_{sphere}) of the pinhole field of view and the true field of view (V_{fov}) as a function of the pinhole aperture angle 2α.

[3] J. Li, R. J. Jaszczak, H. Wang, K. L. Greer and, R. E. Coleman, "Determination of both mechanical and electronic shifts in cone beam SPECT," *Phys. Med. Biol.*, vol. 39, pp. 743–754, 1993.

[4] H. Wang, M. F. Smith, C. D. Stone, and R. J. Jaszczak, "Astigmatic single photon emission computed tomography imaging with a displaced center of rotation," *Med. Phys.*, vol. 25(8), pp. 1493–1501, 1998.

[5] Ph. Rizo, P. Grangeat, and R. Guillemaud, "Geometric Calibration Method for Multiple-Head Cone-Beam SPECT System," *IEEE Trans. Nucl. Sci.*, vol. NS-41(6), pp. 2748–2757, 1994.

[6] F. Noo, R. Clackdoyle, C. Mennessier, T. A. White, and T. J. Roney, "Analytic method based on identification of ellipse parameters for scanner calibration in cone-beam tomography," *Phys. Med. Biol.*, vol. 45, pp. 3489–3508, 2000.